IVYSPRING
INTERNATIONAL PUBLISHER

Theranostics

Research Paper

W-doped TiO₂ nanoparticles with strong absorption in the NIR-II window for photoacoustic/CT dual-modal imaging and synergistic thermoradiotherapy of tumors

Ke Gao[1], Wenzhi Tu[2], Xujiang Yu[1], Farooq Ahmad[1], Xiannan Zhang[1], Weijie Wu[1], Xiao An[2✉], Xiaoyuan Chen[3] and Wanwan Li[1✉]

1. State Key Lab of Metal Matrix Composites, School of Materials Science and Engineering, Shanghai Jiao Tong University, 800 Dongchuan Road, Shanghai 200240, China
2. The Comprehensive Cancer Center, Shanghai General Hospital, Shanghai Jiao Tong University School of Medicine, Shanghai 201620, China
3. Laboratory of Molecular Imaging and Nanomedicine (LOMIN), National Institute of Biomedical Imaging and Bioengineering (NIBIB), National Institutes of Health (NIH), Bethesda, Maryland 20892, United States

✉ Corresponding authors: Prof. Wanwan Li, Email: wwli@sjtu.edu.cn; Prof. Xiao An, Email: 54andromeda@163.com.

Abstract

Multifunctional nanomaterials that have integrated diagnostic and therapeutic functions and low toxicity, and can enhance treatment efficacy through combination therapy have drawn tremendous amounts of attention. Herein, a newly developed multifunctional theranostic agent is reported, which is PEGylated W-doped TiO₂ (WTO) nanoparticles (NPs) synthesized via a facile organic route, and the results demonstrated strong absorbance of these WTO NPs in the second near-infrared (NIR-II) window due to successful doping with W. These PEGylated WTO NPs can absorb both NIR-II laser and ionizing radiation, rendering them well suited for dual-modal computed tomography/NIR-II photoacoustic imaging and synergistic NIR-II photothermal/radiotherapy of tumors. In addition, the long-term in vivo studies indicated that these PEGylated WTO NPs had no obvious toxicity on mice in vivo, and they can be cleared after a 30-day period. In summary, this multifunctional theranostic agent can absorb both NIR-II laser and ionizing radiation with negligible toxicity and rapid clearance, therefore it has great promise for applications in imaging and therapeutics in biomedicine.

Key words: W-doped TiO₂ nanoparticles; second near-infrared (NIR-II) window; multi-model imaging; thermoradiotherapy

Introduction

Cancer is a leading threaten to human health. Currently available clinical treatments [1, 2], such as surgery, radiotherapy, and chemotherapy, typically induce significant side effects [3]. Therefore, noninvasive tumor therapies with high treatment efficacy consistently attract a lot of attention [4, 5]. Multifunctional nanomaterials have drawn more and more interest and have been rapidly developed and employed in cancer diagnostics and therapeutics recent years [6, 7]. The ability of a single structure or particle to display multiple functions (nanotheranostics) [8] enables nanomaterials to be widely used in imaging [9], diagnosis [10], and treatment of cancers [11]. Moreover, single systems that can also provide synergistic therapeutic approaches [7, 12] in addition to multi-modal imaging [13-15] have great potential for developing high efficiency cancer theranostics.

Radiotherapy (RT) that employs x- or γ-rays to destroy cancer cells with no depth restriction is widely used in the clinic [16-18]. However, the side effects of irradiation on normal tissues [19] and low treatment efficacy against hypoxic cancer cells [20] limit the applications of RT. In recent years,

nanomaterials with high-Z elements, such as gold [21], iodine [22], bismuth [23], tungsten [24] and rare earth elements [25], have been demonstrated as excellent radiosensitizers, which can concentrate radiation in tumors, and enhance the efficacy of RT while reduce possible associated side effects [26]. Meanwhile, the combination of RT and photothermal therapy (PTT) can significantly increase the therapeutic efficiency of each alone due to the advantages of these methods and the compensation for the shortcomings of each other [27, 28]. Tumor hyperthermia promotes blood flow and thus improves the oxygen status of cells [29]. However, RT can kill tumor cells out of the range of PTT [16]. Moreover, employment of a radiosensitizer is another way of reducing side effects as it allows the dose of radiation during RT treatment to be decreased [17, 30]. Therefore, a combination of PTT absorption agent in the NIR-II and a radiosensitizer to decrease radiation doses is highly desired, especially for tumors in deep locations.

PTT utilizes the hyperthermia caused by NIR absorption to ablate tumors and is a highly localized and minimally invasive method [31]. Importantly, employment of nanomaterials with high photothermal conversion efficiency in the first NIR window (NIR-I, 650-980 nm) could enhance therapeutic effects [7, 32-36]. However, these effects are limited by the location depth of the tumors, since the laser intensity is inevitably attenuated as the tumor depth increases. Although lasers in the second NIR window (NIR-II, 1000-1700 nm) penetrate deeper and have higher maximum permissible exposures (MPEs) [37], there are fewer reports focusing on PTT in the NIR-II [38-40]. Photoacoustic imaging (PAI) is a newly emergent diagnostic technique. By detecting the ultrasound caused by laser pulses, PAI combines the advantages of traditional ultrasound and optical imaging and has deeper tissue penetration and enhanced spatial resolution [41, 42]. Due to its excellent imaging capabilities, PAI has been applied in molecular, cellular, vascular and tumor imaging [43-46]. Moreover, the specificity and penetration depth of PAI could be further improved through exogenous contrast agents, including small molecule dyes [47-49], inorganic NPs [35, 50-52], and organic NPs [53-55]. The PAI contrast is mainly determined by the optical absorption coefficient which depends on the wavelength of light; therefore, the PTT agents with strong NIR range absorption can be utilized as contrast agents for PAI. Recently, PAI in the NIR-II range has attracted increasing attention due to its stronger penetration ability and higher signal-to-background ratio compared with PAI in the NIR-I [38, 56-58]. Therefore, development of contrast agents with intense absorption in NIR-II is essential for PAI, as well as PTT.

Recently, several types of nanomaterials including noble metal nanomaterials [59, 60], polymer nanocomposites [38, 58] and transition metal sulfide/oxide semiconductors [39, 51], have been reported to respond to NIR-II window as potential photothermal nanomaterials. Semiconductors show significantly different optical bandgaps and free carrier amounts via tuning doping or adjusting stoichiometric ratios, both of which dramatically contribute to semiconductor absorption in the NIR region. As a typical semiconductor, anatase TiO_2 has a wide bandgap energy of 3.2 eV and strong ultraviolet (UV) absorption at around 380 nm. Boron [61], carbon [62], nitrogen [63-65], S [66], Co [67], W [68, 69], Fe [70] and rare earth elements [71, 72] have typically been used as dopants to attenuate the band-gap energy and expand the photoabsorption range of TiO_2 in photocatalysis. Recently, Nb-doped TiO_2 nanocrystals with strong absorption bands in the NIR range, resulted from efficient localized surface plasmon resonances, were obtained due to the considerable free electrons originated from the efficient incorporation of Nb^{5+} ions [73] and can act as excellent nanoagents for PTT in the NIR-II window. Meanwhile, because of the high atomic number of tungsten, tungsten-based nanomaterials have been widely explored as potential contrast agents for computed tomography (CT) [74-76] and radiosensitizers for RT [24]. All these lead us to develop multifunctional W-doped TiO_2 (WTO) nanoparticles (NPs) based on their hypothesized strong absorption band in the NIR range caused by the incorporation of W6+ ions and potential use as high efficiency PTT and PAI contrast agents. Moreover, the presence of tungsten inside NPs may allow utilization as CT imaging contrast and RT agents. So far there are no studies and reports on WTO NP photothermal and radiation properties, and potential applications in multimodel imaging, as well as other biomedical applications.

Herein, a novel WTO NP-based theranostic agent was successfully developed. This theranostic agent has strong absorption property in the NIR-II window, rendering it a potential agent for both dual-modal CT/NIR-II PAI and synergistic PTT/RT of cancer. First, a facile organic route of synthesizing WTO NPs was proposed. The PEGylated WTO NPs product exhibited a strong broad absorption ranging from ultraviolet to NIR wavelengths. A photothermal agent driven by 1064-nm laser with a high photothermal conversion efficiency of 44.8% and excellent photostability was found to be a successful approach. The WTO NPs also showed application

potential as in vivo contrast agents for CT and NIR-II PAI based on their great X-ray attenuation coefficient of W and strong absorption in the NIR-II range. PEGylated WTO NPs were also combined with RT and PTT for tumor treatment in tumor-bearing mice and showed dramatic synergistic effects. Furthermore, PEGylated WTO NPs displayed both low toxicity and excellent biocompatibilities *in vivo*. Our results highlight the potential future applications of WTO NPs as well as other multifunctional nanomaterials in cancer diagnostics and therapy based on the doped semiconductor NPs for cancer theranostics.

Results and Discussion

Synthesis and Characterization of Nanoparticles

WTO NPs were successfully synthesized through a facile modified organic route [73]. Briefly, tetraethyl titanate $[Ti(OC_2H_5)_4]$ and tungsten (VI) chloride (WCl_6) were heated to 290°C for 1 hour in an anhydrous and oxygen-free system consisting of 1-octadecanol, oleic acid, and 1-octadecene. Under these conditions, several WTO samples were doped with different amounts of W (TiO_2: 5 at% W, TiO_2: 10 at% W, TiO_2: 15 at% W, and TiO_2: 20 at% W) by changing the molar ratio of $WCl_6/Ti(OC_2H_5)_4$ in the precursor solution. Undoped TiO_2 NPs were also prepared in the absence of WCl_6 precursor for comparison. The morphologies of these samples were assessed by transmission electron microscopy (TEM).

As shown in **Figure 1a** and **Figure S1**, the as-prepared TiO_2 NPs (15 at% W) were not uniform in shape, which included primarily "rice grains" with lengths of 9.1 ± 2.2 nm and diameters of 5.7 ± 1.4 nm. In our work, we tried to dope WTO nanoparticles using W precursor concentration as high as possible to ensure enough W inside the WTO nanoparticles for effective CT imaging and RT. As shown in **Figure S1**, with the increase of doping concentration of W, the morphology of the nanoparticles changes gradually. When the W doping concentration is 15 at%, the uniformity of resultant WTO NPs can be maintained. However, the uniformity of WTO NPs becomes poor when the W doping concentration is higher than 15 at%. Therefore, WTO NPs with W doping concentration of 15 at% were used for further investigation. High-resolution TEM (HRTEM) images of TiO_2: 15 at% W (inset of **Figure 1a**) reveal lattice fringes with an interplane spacing of 0.358 nm corresponding to the (002) plane of anatase TiO_2. All the samples had similar X-ray powder diffraction (XRD) patterns and yielded six peaks at 25.3°, 37.8°, 48.0°, 53.9°, 55.1°, and 62.7° corresponding to the (101), (004), (200), (105), (211), and (204) planes of anatase TiO_2 (JCPDS no. 21-1272), respectively (**Figure 1b**, a). These results indicate W-doping does not change the crystal phase of anatase TiO_2 [77], which may be attributed to the similar ionic radii of W^{6+} (0.60 Å) and Ti^{4+} (0.605 Å)[78]. Moreover, as shown in **Figure S2**, the distributions of Ti, W, and O in the TiO_2: 15 at% W NPs were homogeneous, indicating successful doping with W. The chemical states of W
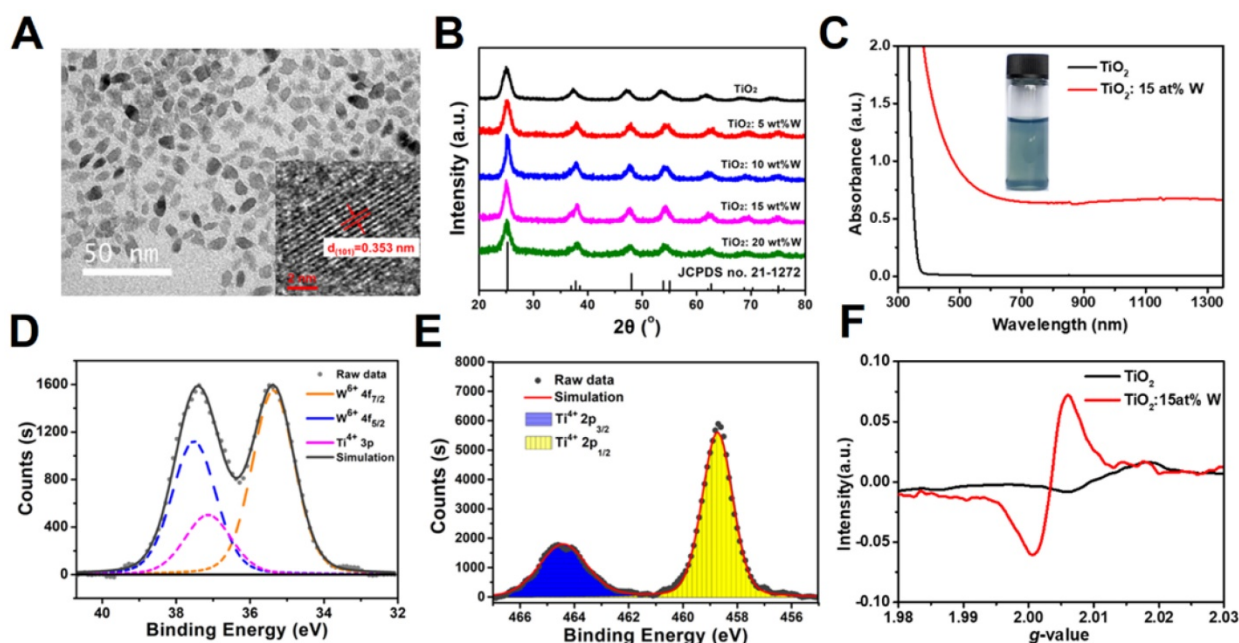

Figure 1. (A) TEM image of TiO_2: 15 at% W. Inset shows the HRTEM image. (B) XRD patterns of TiO_2 and W-doped TiO_2. (C) UV-vis-NIR spectra of TiO_2 and TiO_2: 15 at% W dispersed in chloroform (Ti concentration = 600 μg mL⁻¹). Inset shows the color. (D, E) XPS fitting spectra of (D) W4f and (E) Ti2p. (F) EPR spectra of TiO_2 and TiO_2:15 at% W.

and Ti in the TiO$_2$: 15 at% W NPs were assessed by XPS, which confirmed the valence of W was +6 **(Figure 1d)** and Ti was +4 **(Figure 1e)**.

UV-vis-NIR spectra were applied to characterize the optical properties of these samples. As shown in **Figure 1c**, the intrinsic TiO$_2$ NPs dissolved in chloroform only absorbed ultraviolet light, while the deep blue WTO NP solution exhibited a strong and continuous absorption from visible light to NIR (>1350 nm) without yielding any sharp peaks outside of the intense UV absorption. The expansion of photoabsorption could be attributed to the increase in free carrier concentration as revealed by the electron paramagnetic resonance (EPR) spectra **(Figure 1f)**. Specifically, the peak around 2.01 eV was related to the WTO NP electrons. The doped W^{6+} replaced Ti^{4+}, releasing electrons to form free carriers and additional electronic states between the conduction and valence bands of the TiO$_2$ and thus expanding the absorption spectrum from the ultraviolet to NIR range. Functional groups on the surface of the NPs are important for biomedical applications. Coating of WTO NPs with a hydrophilic layer was performed at room temperature via sonication with a DSPE-PEG$_{5000}$ solution. The surface modification was investigated by FTIR and the intensities of the C-O-C stretch band (1101 cm^{-1}) displayed a distinct increase after coupling based on the DSPE-PEG$_{5000}$ peak **(Figure S3)**. The morphology of the PEGylated WTO NPs was confirmed by TEM **(Figure S1b)**, where little change was observed compared to those without PEG coating. Moreover, the PEGylated WTO NPs were also proved to have excellent stability and dispersibility in different kinds of physiological media **(Figure S4)** with hydraulic radii of ~47 nm **(Figure S5)**, suggesting that NPs have been successfully modified for potential further use both *in vitro* and *in vivo*. In addition, the aqueous PEGylated WTO solution maintained the optical absorption properties and the absorption intensity increased as the NP concentration increased **(Figure S6)**.

In vitro **Photothermal Performance**

The PEGylated WTO NPs showed a strong and continuous absorption from visible light to NIR (>1350 nm), exhibiting no sharp peaks, which led us to apply a common laser with a 1064-nm wavelength to trigger the NIR-II PTT. The photothermal properties of the NPs were first assessed via examination of the temperature variation in NP solution containing different concentrations of Ti (0, 25, 50, 100, and 200 ppm) irradiated using a 1064-nm laser. The temperature variation for 1 mL NP solution in plastic tubes was recorded during the irradiation (300 seconds, 1 W cm^{-1}). **Figure 2a** shows that the

water temperature increased by only 5°C and the PEGylated NP solution exhibited a concentration-dependent temperature enhancement. As the concentration of Ti increased from 25 to 200 ppm, the final temperature change (ΔT) increased from ~9 to ~24 °C. The stability of the photothermal conversion of the WTO NPs was evaluated next using a cycle experiment. WTO NP solution (1 mL, 100 ppm) were irradiated with a 1064-nm laser at 1 W cm^{-1} for 5 minutes and then the laser was turned off to let the solution cool to 26°C. As shown in **Figure 2b**, the change in temperature was almost the same during each laser on-off cycle, indicating the WTO NPs had excellent photothermal stability. Photothermal conversion efficiency (η) is an important parameter for evaluating photothermal agents and can be calculated as described previously [79]. The η value of the PEGylated WTO NPs was 44.8% at 1064 nm **(Figure 2c and 2d)**, which is higher than the reported η values of other PTT agents in the NIR-II window [39, 59, 80, 81].

In vitro **Cytotoxicity Assay and Cellular Uptake**

TiO$_2$ is an environmentally friendly material and white TiO$_2$ and black H-TiO$_2$ NPs are considered to also have low toxicity and good biocompatibility [82]. Here, we investigated the cytotoxicity of PEGylated WTO NPs with a CCK-8 assay. As can be seen in **Figure 2e**, PEGylated WTO NPs caused no significant 4T1 cell cytotoxicity as the relative viability was higher than 85% even with treatment of 200 μg mL^{-1}·Ti. Moreover, **Figure S7** shows the intracellular uptake of PEGylated WTO NPs, the cellular internalization was enhanced with the increasing incubated time, and the concentration of Ti in cells reached a relatively saturated level after 8 hours of incubation. The characteristics of PEGylated WTO NPs including high η value, low cytotoxicity, great photothermal stability, and strong penetration capability in tissue make them promising photothermal agents for application in NIR-II window.

Clonogenic Assays

After demonstrating the ability of PEGylated WTO NPs to trigger PTT, a clonogenic survival assay was carried out to determine whether PEGylated WTO NPs can enhance RT efficacy. As shown in **Figure 2f**, WTO NPs enhanced radiotherapy when the concentration of W was 100 ppm. The SF$_2$ value, which indicates the cell survival fraction when the radiation dose is 2 Gy, was 0.553 for the combination treatment group and 0.799 for the group lacking WTO NPs **(Table 1)**. The SER10 was 1.323 when the SF value was 0.1, which is higher than that of AuNPs

(1.19) and similar to that of paclitaxel (1.32) [83], demonstrating significant radiosensitization by PEGylated WTO NPs.

Table 1. Parameters and fitted formulas for *in vitro* radiation therapy with and without WTO NPs.

	D_0	D_q	SF_2	SER10	fitted formula
RT	4.520	2.483	0.799	-	$SF=1-(1-e^{-0.4186*D})^{2.828}$
RT + WTO	2.907	0.808	0.533	1.323	$SF=1-(1-e^{-0.4427*D})^{1.430}$

In vitro Photothermal Therapy and Radiation Therapy

To test the therapeutic efficiency of PEGylated WTO NPs *in vitro,* different therapeutic experiments in cellular levels were performed. As shown in **Figure S8**, NIR alone and X-ray alone treatment decreased 4T1 cell viability to 93 and 85%, respectively, while the PTT effect and the RT effect of WTO nanoparticles can result in the obvious decrease of the cell viability to 62 and 51%. When the PTT effect combined with RT effect, it was found that cell viability substantially decreased to 21%, confirming the considerable WTO nanoparticles enhanced RT/PTT synergistic effect *in vitro*, which encouraged us to further study the synergistic therapeutic effects of photothermal and radiotherapy through animal models.

In vivo Blood Circulation and Tumor Accumulation

Motivated by the experimental results *in vitro*, we next examined the pharmacokinetic behavior and tumor accumulation pattern of PEGylated WTO NPs (3 mg/mL, 200 μL) in tumor-bearing mice using intravenous (i.v) administration. For the pharmacokinetic study, we took blood samples at different time points, followed by inductively coupled mass spectrometer (ICP-MS) analysis to measure the amount of Ti. As shown in **Figure S9**, the content of PEGylated WTO NPs in the blood of mice gradually decreased with time. And the half-decay time of PEGylated WTO NPs circulating in the blood was approximately 1.28 hours, indicating that the WTO NPs modified by mPEG-DSPE possess well biocompatibility and could cycle in the blood for a period of time, which is conducive to the enrichment of nanomaterials at tumor site. Then we further studied the biodistribution of PEGylated WTO NPs on 4T1 tumor bearing mice. As shown in **Figure S10**, 24h after tail-vein injection, NPs mainly concentrated in spleen, liver and kidney, the enrichment percentage of PEGylated WTO NPs at the tumor site is about 5% injected dose per gram (ID g^{-1}) due to the enhanced permeability and retention (EPR) effect.
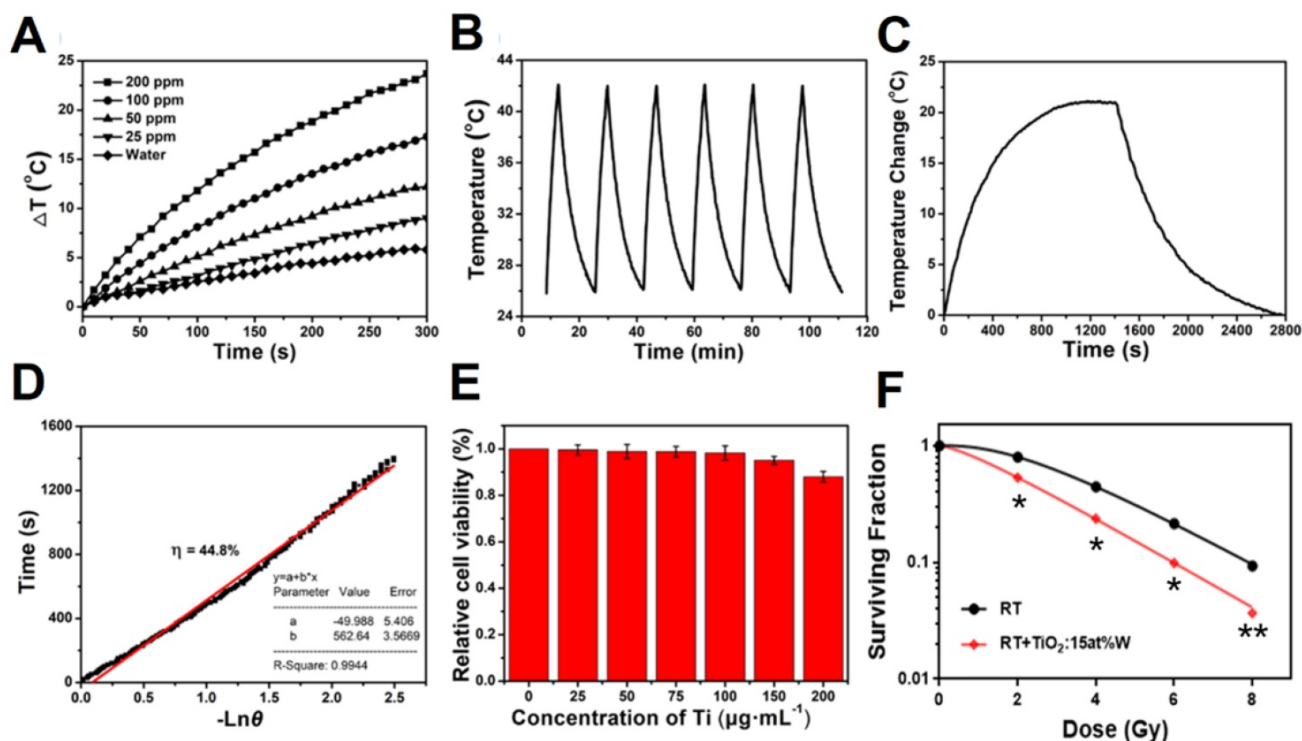

Figure 2. (A) Temperature changes of WTO NP solution with different concentrations of Ti under 1064-nm laser irradiation at 1 W cm^{-2} for 5 minutes. (B) Temperature changes of a WTO NP solution with a Ti concentration of 200 ppm over six cycles under 1064-nm laser irradiation at 1 W cm^{-2}. (C) Temperature profile of a WTO NP solution with a Ti concentration of 100 ppm over 2800 s under 1064-nm laser irradiation at 1 W cm^{-2} for about 1400 s. (D) Calculation of time constant for heat transfer from the system using linear regression of the cooling profile. (E) Relative viabilities of 4T1 cells treated with WTO NPs with different concentrations of Ti for 24 h were evaluated using CCK-8 assay. (F) Inhibitory effect of WTO NPs (0 or 100 ppm of Ti) on 4T1 cells under different irradiation dosages. (*p<0.05,**p<0.01)
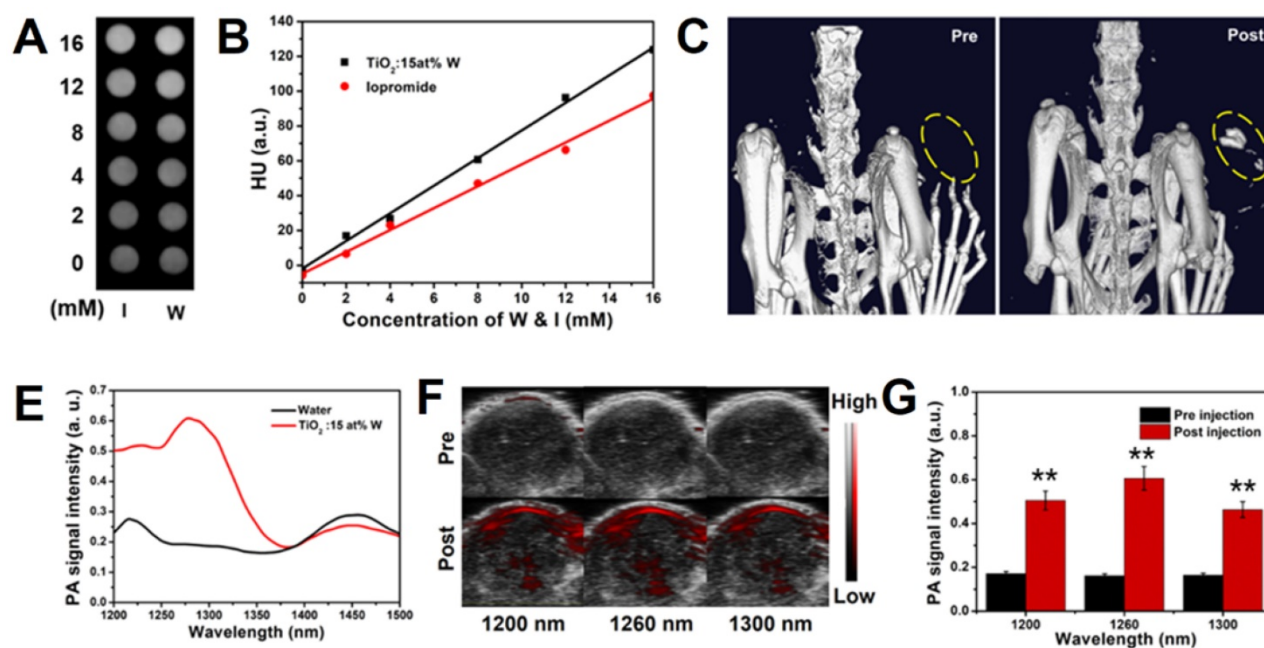
Figure 3. (A) *In vitro* CT images of iopromide (upper row) and WTO NP solution (lower row) of different concentrations. (B) HU values of various concentrations of WTO NP and iopromide solution. (C) *In vivo* CT images of mouse pre- (left) and post-intratumoral (i.t.) injection (right) with WTO NP solution. (D) *In vitro* PA signal intensity of WTO NP solution (0.5 mg mL^{-1} of Ti) and water from 1200 to 1500 nm. (E) *In vivo* ultrasonic PA composite images pre- (upper row) and post- (lower row) i.t. injection of WTO NP solution at 1200, 1260, and 1300 nm. (F) *In vivo* PA signal intensity of tumors pre- (black) and post-i.t. injection (red) of WTO NP solution(****p<0.01).

In vitro and *In vivo* X-ray Computed Tomography

The dramatic photoelectric and NIR absorbance of the W atoms in the PEGylated WTO NPs under the radiation of X-ray them to be potentially applied in tumor PTT, PA/CT dual-modal imaging, and sensitizing RT. To evaluate the performance of PEGylated WTO NPs in CT imaging as a contrast agent *in vitro*, a commonly used CT contrast agent of iopromide in clinic was employed for comparison. As shown in **Figure 3a**, both the WTO and iopromide solution exhibited concentration-dependent signal enhancement, but the PEGylated WTO group showed a higher signal intensity than the corresponding iopromide group when the W and I concentrations were equal. Quantification of signal intensity revealed the slopes of the CT values of the PEGylated WTO NPs and iopromide were ~7.9 and ~6.3, respectively **(Figure 3b)**. The beneficial effect of using PEGylated WTO NPs in CT imaging *in vitro* encouraged us to assess their use with CT imaging in 4T1 tumor-bearing mice. As illustrated in **Figure 3c**, the CT value of the tumor region (yellow dashed circle) for the tumor to be visualized before i.t. injection. Upon injection of 30 μL of PEGylated WTO NPs with 6 mg mL^{-1} of W, tumor displayed clear contrast with a white area. This observed increase suggests PEGylated WTO NPs could be used as an effective CT contrast agent.

In vitro and *In vivo* Photoacoustic Imaging

PAI employs laser to acoustically visualize biological tissues, therefore it possesses unique spatial resolution and high imaging depth, especially in the NIR-II window. For NIR-II PAI *in vitro*, we collected photoacoustic images of PEGylated WTO solution (0.5 mg mL^{-1}) and deionized water in micro polyurethane tubing from 1200 to 1500 nm. We quantified the signal intensity of the photoacoustic images from 1200 to 1500 nm **(Figure 3d)** and found the PA signal of the PEGylated WTO NPs solution was 2-3 times stronger than that of water with a wide wavelength range between 1200 and ~1325 nm. As shown in **Figure S11**, the PEGylated WTO NPs displayed strong PA signals at 1200, 1260, and 1300 nm, while the water group yielded weak signals that were almost not visible in images taken at the same wavelength. The *in vivo* tumor PAI efficiency was assessed by calculating the PA values of the mice bearing 4T1 tumors after i.t. administration of PEGylated WTO NPs **(Figure 3e)**. The mice bearing 4T1 tumors were PA imaged prior to i.t. injection of PEGylated WTO NPs as a control and there was no obvious photoacoustic signal present except for a low signal from the skin. By contrast, intense photoacoustic signals were detected from the tumor at 1200, 1260, and 1300 nm after injection. The signal quantization results shown in **Figure 3f** demonstrate the PA signals of the post-injection group were approximately 2.95- (1200 nm), 3.75- (1260 nm), and 2.82-time (1300 nm) that of

the pre-injection group, indicating PEGylated WTO NPs are also suitable for PAI as a contrast agents in a wide range of NIR-II wavelengths.

NIR-II Photothermal and Radiotherapy *In Vivo*

We next evaluated the *in vivo* anti-cancer efficacy of the PEGylated WTO NPs in a 4T1 tumor-bearing mouse model. Mild tumor hyperthermia was induced by administering a low dose sample and then combination treatment of PTT/RT was applied to evaluate their effect. 4T1 tumor-bearing BALB/c nude mice were randomly divided into five groups (n=5) to study different treatments. For the PTT, we recorded infrared videos of mice during NIR-II laser irradiation **(Figure 4a)**. After quantification of the infrared images, we illustrated temperature variation on the tumor surfaces **(Figure 4b)**. Under a 1064-nm laser irradiation at 0.5 W cm^{-2}, the temperature of the NP-injected groups increased to ~45°C in 5 min and was maintained for 15 min, which guaranteed mild tumor hyperthermia, while the PBS-injected group exhibited only a 40°C maximum temperature **(Figure 4a and b)**. A similar phenomenon was observed for the groups treated with radiotherapy, but not NIR
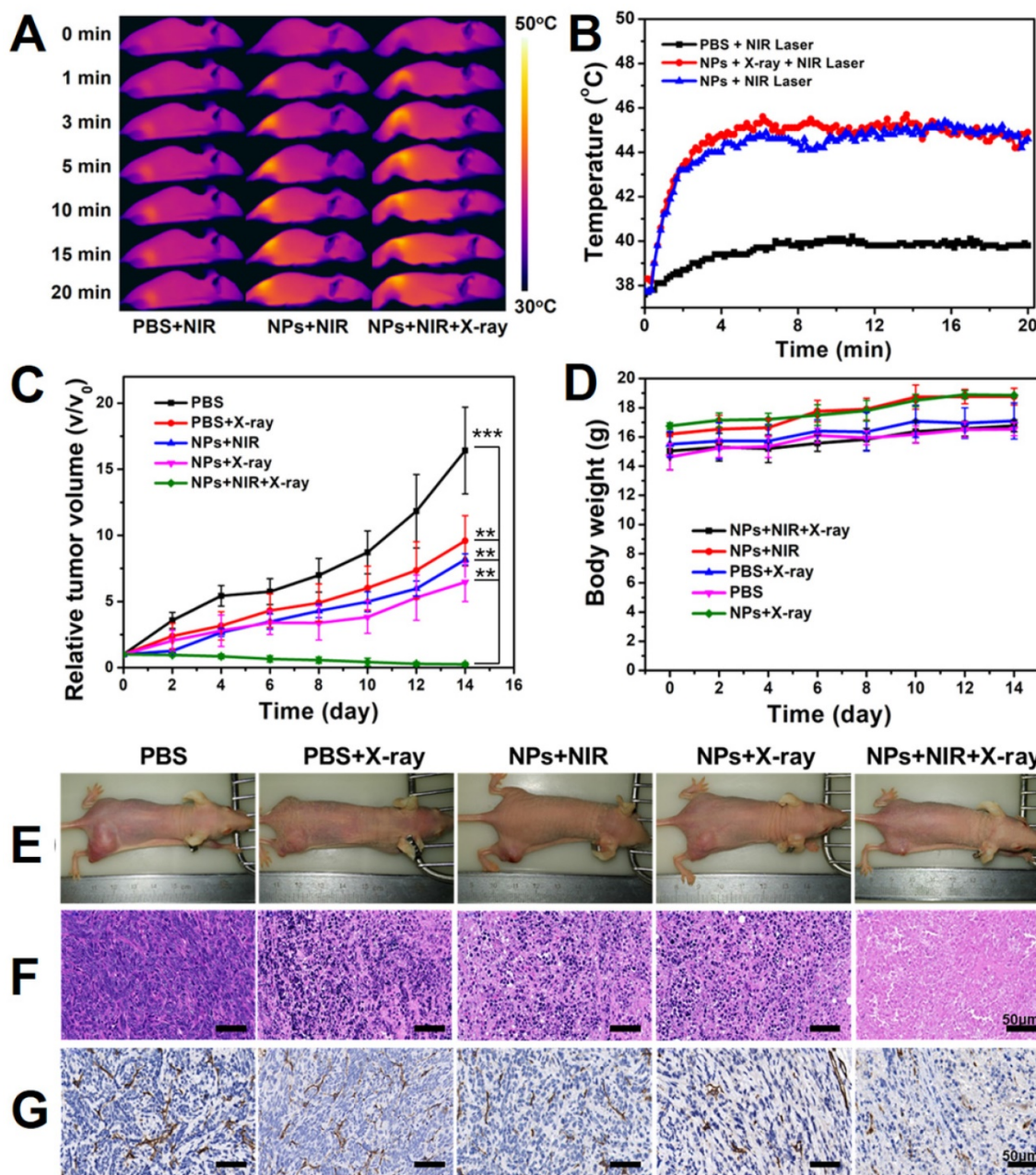

Figure 4. (A) Temperature variation on the surface of tumors in mice under laser irradiation of 1064 nm after i.v. injection with PBS or WTO NP solution. (B) Infrared images of mice under 1064 nm laser irradiation after i.v. injection with PBS or WTO NP solution. (C) Tumor volume and (D) body weight variation curves of mice in each group. (E) Photographs of mice 14 days after exposure to different treatments. (F) H&E and (g) CD31 staining of tumor sections 24 h after exposure to different treatments (**p<0.01, ***p<0.005).

laser irradiation, and tumor growth was only slightly inhibited. Notably, the growth rate of the group treated with NP injection and X-ray irradiation was lower than that of the group receiving PBS injection and X-ray irradiation, confirming enhancement of RT by the PEGylated WTO NPs. Compared with the groups only treated with PTT or RT, the group receiving the combination therapy of NP injection and NIR-II laser and X-ray irradiation exhibited significant inhibition of tumor growth. By contrast, the control tumors displayed uninhibited growth in the PBS group **(Figure 4c and e)**.

To identify the changes inside the tumors, we stained tumor slices using hematoxylin and eosin (H&E, see **Figure 4f**) and also incubated with anti-CD31 antibody **(Figure 4g)**. We observed remarkable damage of tussues and significant tumor angiogenesis suppression in PTT/RT combination treatment group only, consistent with the anti-cancer effect of the PTT/RT combination treatment mentioned above. Moreover, no significant loss of body weight and death of mice were observed, and all of the mice behaved normally **(Figure 4d)**. Our results demonstrate that PEGylated WTO NPs can be used as excellent agents for NIR-II PTT and RT, furthermore, when these therapies were used together, there are synergistic effects against tumors.

Blood Panels and Histological Examinations *In vivo*

Considering that accumulation of NPs in vivo might induce unwanted side effects or toxicity after a long-term treatment, we next evaluated the potential long-term toxicity of PEGylated WTO NPs *in vivo*. After intravenous injection of PEGylated WTO NPs for 1, 7, and 30 days, mice were sacrificed, complete blood panel and blood biochemistry analyses were performed and major organs (liver, heart, lungs, spleens and kidneys) were harvested for ICP-AES and H&E staining. The complete blood panel measured the albumin/globin ratio (A/G), blood urea nitrogen (BUN), red blood cell (RBC), white blood cell (WBC), hematocrit (HCT), hemoglobin (HGB), mean corpuscular hemoglobin concentration (MCHC), mean corpuscular volume (MCV), mean corpuscular hemoglobin (MCH), and platelet count (PLT). (**Figure 5a**). Although the BUN, WBC, RBC, HGB, HCT, and PLT levels decreased slightly 1 day after administration of PEGylated WTO NPs, the values returned to normal levels by days 7 and 30. All other parameters were normal. The blood chemistry analysis including aspartate aminotransferase (AST), alkaline phosphatase (ALP), and alanine aminotransferase (ALT) was carried out and no abnormalities were detected compared with the control group, suggesting that the PEGylated WTO NPs caused no obvious liver toxicity (**Figure 5b**). In addition, neither visible inflammation nor organ damage was observed from the H&E staining images of tumors **(Figure S12)** from either the treatment and control groups. By measuring the Ti content in major organs by ICP-AES **(Figure 5c)**, we found the injected NPs mainly accumulated in the spleen and liver, while the heart, lungs, and kidneys displayed relatively low Ti accumulation levels. The Ti content decreased in all organs over time and became relatively low at 30 d post-injection. These results confirmed the low long-term toxicity and excellent biocompatibility of the PEGylated WTO NPs *in vivo*.

Conclusions

In summary, we showed that PEGylated WTO NPs with diameters averaging ~10 nm could be facilely synthesized via an organic route. PEGylated WTO NPs had strong absorbance in the NIR-II window due to successful doping with W, therefore exhibiting excellent NIR-II photothermal properties and photostability. Following modification with DSPE-PEG5000, the resulting PEGylated WTO NPs became an excellent candidate agent for dual-modal CT/NIR-II PAI. In addition, PEGylated WTO NPs had the beneficial properties of absorbing both NIR-II laser radiation and ionizing radiation, as well as enhancing RT efficacy. We showed that these NPs can result in a dramatic synergistic effect on RT and PTT for tumor treatment *in vivo*. In contrast, treatment with RT or PTT alone can partially suppress tumor growth. The long-term clearance and toxicity results showed that PEGylated WTO NPs can be completely cleared within 30 days in mice without obvious toxicity. In summary, this promising theranostic agent with its excellent imaging and therapeutic properties coupled with its low toxicity and reasonable clearance has great promise for use in the field of biomedical science.

Materials and Methods

Materials

Tungsten (VI) chloride and 1-octadecanol were purchased from Macklin (Shanghai, China). Oleic acid and 1-octadecene were obtained from Sigma Aldrich. Titanium (IV) ethoxide was purchased from Alfa Aesar (UK). DSPE-PEG$_{5000}$ was purchased from Shanghai Yudu Biotechnology (China). Acetone, hexane, and chloroform were purchased from Yonghua Chemical Technology (Jiangsu, China). Iopromide injection was purchased from Bayer Pharma AG (Germany). The 4T1 cells were provided by the Shanghai Center for Systems Biomedicine
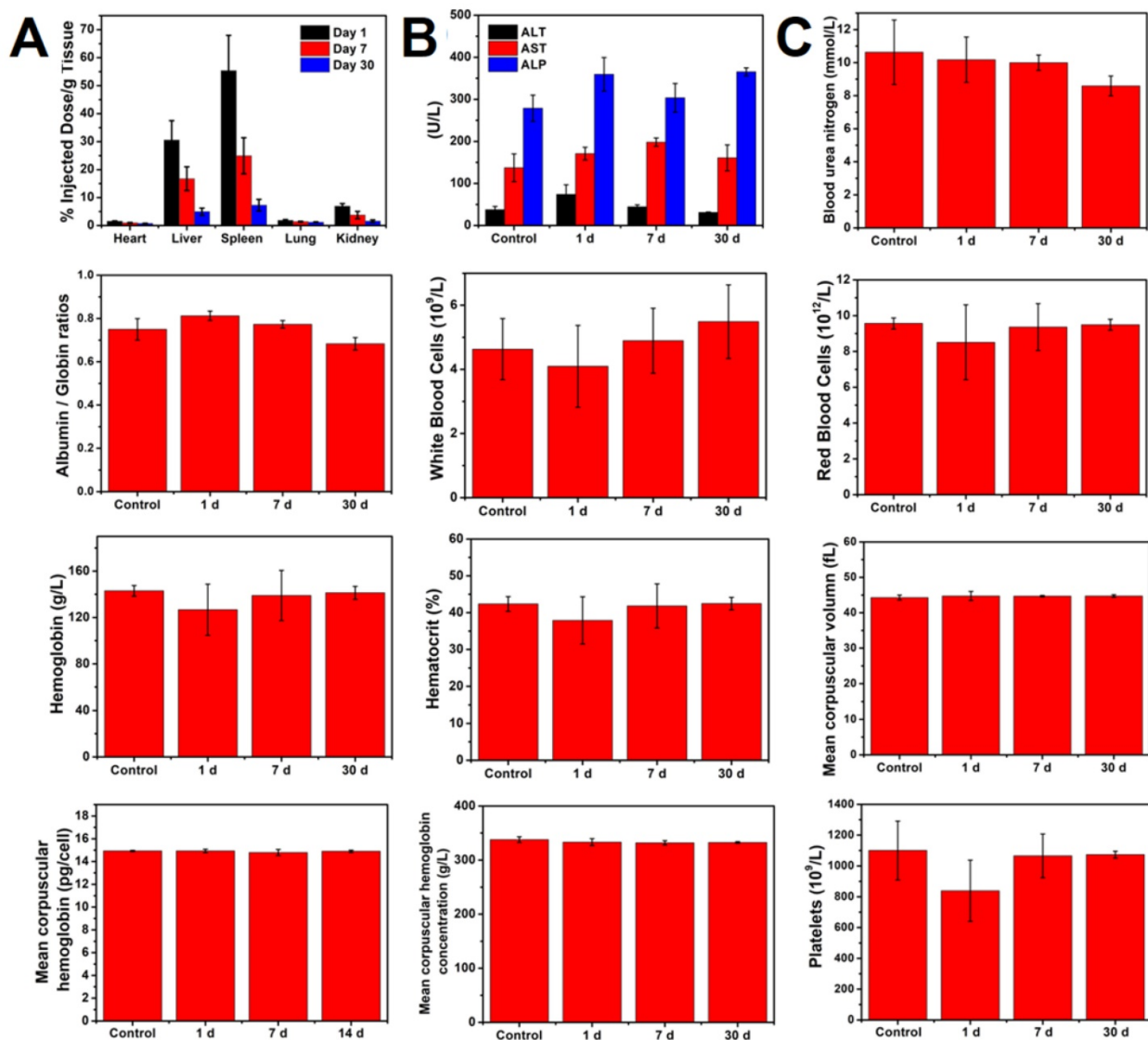
Figure 5. (A) Biodistribution of WTO NPs in organs of mice sacrificed at different time points. (B) Blood biochemistry ALT, AST, and ALP analysis of mice sacrificed at different time points. (C) Hematology analysis of eight blood panel parameters of mice sacrificed at different time points.

(Shanghai, China). A cell counting kit-8 (CCK-8) kit was obtained from BBI Solution (UK). Female BALB/c nude mice of 5~6 weeks old were obtained from Slac Laboratory Animal Center (Shanghai, China).

Synthesis of WTO NPs

Under a vacuum at 110°C for 1 h, 20 mmol of 1-octadecanol was dissolved in a mixture of 1-octadecene (7 mL) and oleic acid (3 mL) in a 25 mL three-neck flask connected to a Schlenk line. Then, the solution was heated to 130°C under a nitrogen atmosphere and maintained for 30 min to reach an anhydrous, oxygen-free state. Next, 2 mmol of tetraethyl titanate and 0.3 mmol of tungsten (VI) chloride dissolved in 10 mL methanol was injected into the three-neck flask once the solution had cooled to 80°C. When the methanol had completely

evaporated, the temperature of the system was raised to 290°C and maintained for 1 h. Acetone and n-hexane were then added to wash the precipitate and then the solution was centrifuged to obtain NPs, followed by redispersion in chloroform.

PEGylation of Nanoparticles

Chloroform solution (2 mL) containing 10 mg of NPs was mixed with 5 mL chloroform solution containing 20 mg DSPE-PEG$_{5000}$ in a 25-mL three-neck flask. After stirring in the presence of continuous nitrogen gas at room temperature overnight, the chloroform was evaporated. Deionized water (2 mL) was added to the flask to redisperse the NPs. After sonicating for 5 minutes, PEGylated NPs were completely dissolved in water and became hydrophilic. To remove large aggregates that possibly formed during surface modification, the aqueous

solution was centrifuged at 3000 rpm for 10 min. The final product was stored at 4°C until use.

In vitro Photothermal Property

To evaluate the photothermal performance of the NPs, 1 mL aqueous solution containing various concentrations of NPs was added to plastic tubes and then irradiated with a 1064-nm laser. Temperature variation and thermal photos were recorded with an FLIR E50 thermal camera.

In vitro Cytotoxicity Assay and Cellular Uptake

The cytotoxicity of PEGylated NPs was evaluated using CCK-8 assays. The 4T1 cells were plated in 96-well plates at 7×10^3 cells per well and incubated for 24 h. The culture media were then replaced with fresh culture media containing NPs and different concentrations of Ti (0, 25, 50, 75, 100, 150, and 200 μg mL^{-1}) and incubated for another 24 h. Finally, cells were washed with fresh media to remove the NPs and cell viability was examined using a CCK-8 assay.

In order to study the ability of 4T1 cells to internalize WTO NPs, 4T1 cells were grown in six well plates (1×10^5 cells/well) for 24 h. The culture media were then replaced with culture media containing WTO NPs with a Ti concentration of 100 ppm and the plates were then incubated at 37 °C for a series of time (0.5, 1, 2, 4, 8, and 12 h). Following this incubation, cells were washed with PBS three times and released with cell dissociation buffer. Finally, cells were centrifuged and then digested by concentrated aqueous HNO$_3$. The amount of Ti was then analyzed using ICP-MS.

Clonogenic Assays

To measure the radiosensitization by NPs, two groups of 4T1 cells were plated in six-well plates at different densities (100, 200, 500, 1000, and 2000 cells/well) and incubated for 24 h. The culture media were then replaced with fresh media containing NPs and different concentrations of W (0 or 100 μg mL^{-1}). After incubating for another 24 h, the plates were irradiated with different doses of X-rays (0, 2, 4, 6, and 8 Gy). Thereafter, the cells were incubated with fresh media for another 10 days under standard conditions. Finally, the surviving colonies were enumerated and used plating efficiency (PE), surviving fraction (SF), and sensitizer enhancement ratio (SER) were calculated.[84] SER10 refers to the sensitizer enhancement ratio at 10% cell survival and is critical for evaluating the radiosensitization effect of a radiosensitizer.[83, 85] The D_0 and N values were calculated from the fitting results of a multitarget single-hit model, $SF = 1-(1-e^{-D/D0})^N$.

$$PE = \frac{\text{Number of colonies formed}}{\text{Number of cell seeded}} \times 100\%$$

$$SF = \frac{\text{Number of colonies formed after treatment}}{\text{Number of cell seeded} \times PE} \times 100\%$$

$$SER = \frac{D \text{ (control group)}}{D \text{ (experimental group)}}$$

In vitro Photothermal Therapy and Radiation Therapy

To test the therapeutic efficiency *in vitro*, 4T1 cells wre cultured in 96-well plates at a density of 7×10^3 cells per well for 24 h. After the cells had grown to the full bottom of the plates, the cells were set to eight groups (control, X-ray, NIR-II, NPs, NPs+NIR, NPs+X-ray, NIR+X-ray and NPs+NIR+X-ray). The meda were replaced by fresh meda or media containing WTO NPs with a Ti concetration of 100 ppm. Followed incubation for 8h, 4T1 cells were treated with 1064 nm laser (1 W cm^{-2}, 10 minutes) or X-ray (4Gy) respectively and then incubated for 24h. Finally, cells were washed with fresh media to remove the NPs and cell viability was examined using a CCK-8 assay.

Animal Experiments

All animal operations were in accordance with Shanghai Jiao Tong University institutional regulations regarding animal use and care. Tumors were established by subcutaneously injecting of 2×10^6 4T1 cells (in 60 μL PBS) into their right legs of nude mice. The treatments were started when the tumor volume (volume = length × width^2/2) reached approximately 60 mm^3.

In vivo Blood Circulation and Tumor Accumulation

A PBS solution of WTO NPs (200 μL, 3 mg mL^{-1} of Ti) was injected intravenously into healthy mice (n=5). Blood was then collected from the eyelids of mice at different time points (5 min ,0.25, 0.5, 1, 2, 4, 8, 12 and 24 h) after injection. Finally, samples were digested by aquous HNO$_3$ before the amount of Ti was measured by ICP-MS.

4T1 tumor-bearing BALB/c mice were intravenously injected with 200 μL of WTO NP solution (3 mg mL^{-1} of Ti) and euthanized after 24 h, respectively (n = 5). Tumors and main organs were collected and then digested by concentrated aquous HNO$_3$ overnight before the amount of Ti was measured by ICP-MS.

In vitro and *in vivo* X-ray Computed Tomography

To evaluate the CT imaging performance of NPs *in vitro*, iopromide was used for comparison. NP

solution (200 μL) containing different concentrations of tungsten or iodine (0, 2, 4, 8, 12, or 16 mM) were CT imaged with a GE light-speed VCT at 80 kV and 500 mA with a 0.625 mm slice. Iopromide solution containing the corresponding concentrations of I were set as the control.

For *in vivo* CT imaging, nude mice were anesthetized by intraperitoneal injection of pentobarbital sodium solution. Then CT images of the mice before and after intratumoral (i.t.) injection of WTO solution were acquired using the Quantum GX.

In vitro and *in vivo* Photoacoustic Imaging

To evaluate the *in vitro* photoacoustic imaging performance of the NPs, we used micro polyurethane tubing to hold a NP solution with 0.5 mg mL^{-1} Ti and deionized water as a control. Then a multimode small animal ultrasound/photoacoustic imaging system was employed to collect both photoacoustic and ultrasonic images and then the photoacoustic signals were quantified by VevoLAB software at an excitation of 1200 to 1500 nm.

For *in vivo* photoacoustic imaging, nude mice were anesthetized and photoacoustic and ultrasonic images of tumors both before and after i.t. injection of 30 μL of PEGylated NPs with 1 mg mL^{-1} Ti were acquired using the multimode small animal ultrasound/photoacoustic imaging system.

NIR-II Photothermal and Radiotherapy *in vivo*

For *in vivo* therapy assessment of NPs, 4T1 tumor-bearing BALB/c nude mice were randomly divided into 5 groups (n=5): (I) PBS injection, (II) PBS injection + X-ray, (III) NP injection + NIR laser, (IV) NP injection + X-ray, and (V) NP injection + NIR laser + X-ray. First, the mice in each group were intravenously injected with 200 μL of PBS or NP solution with a Ti concentration of 3 mg mL^{-1}. After 24 h, groups III and V were treated with 1064-nm laser irradiation (0.5 W cm^{-2}, 20 minutes), while groups II, IV, and V were treated with X-rays (4 Gy). During the laser irradiation, an infrared thermal video of each mouse was recorded and the temperature of the tumors was also captured in real time. At 24 h after treatment, one mouse in each group was sacrificed and the tumors were harvested, sliced, and stained with H&E and CD31. For long-term observation, the mice body weights and tumor sizes were recorded every two days for a total of 14 days.

Histological Examinations and Blood Panels

Twenty mice were randomly divided into four groups (n=5). Three groups of mice were intravenously injected with 200 μL NP solution with 3 mg mL^{-1}Ti, while the mice in control group were intravenously injected with 200 μL PBS. For the first three groups, the mice were sacrificed 1, 7, and 30 days after injection. Blood was collected in anticoagulant-containing tubes for hematological analysis and the livers, hearts, lungs, spleens, and kidneys were collected for ICP-AES and H&E staining.

Abbreviations

PEG: polyethylene glycol; WTO: W-doped TiO$_2$; NPs: nanoparticles; NIR-II: the second near-infrared; RT: Radiotherapy; PTT: photothermal therapy; NIR-I: the first NIR window; MPEs: maximum permissible exposures; PAI: photoacoustic imaging; UV: ultraviolet; CT: computed tomography; XRD: X-ray powder diffraction; TEM: transmission electron microscopy; HRTEM: hgih resolution transmission electron microscopy; XPS: X-ray photoelectron Spectroscopy; UV-vis: ultraviolet-visible; EPR: the electron paramagnetic resonance; DEPE-PEG5000: 1,2-distearoyl-sn-glycero-3-phosphoethanolamine-pol yethylene glycol-5000; FTIR: fourier-transform infrared spectroscopy; CCK-8: cell counting kit-8; H&E: hematoxylin and eosin; A/G: albumin/globin ratio; BUN: blood urea nitrogen; RBC: red blood cell; WBC: white blood cell; HCT: hematocrit; HGB: hemoglobin; MCHC: mean corpuscular hemoglobin concentration; MCV: mean corpuscular volume; MCH: mean corpuscular hemoglobin; PLT: platelet count; AST: aspartate aminotransferase; ALP: alkaline phosphatase; ALT: alanine aminotransferase; ICP-MS: inductively coupled plasma-mass spectrometer; PE: plating efficiency; SF: surviving fraction; SER: sensitizer enhancement ratio; PBS: phosphate buffer saline.

Supplementary Material

Additional characterization and results: TEM images, elemental maps, FTIR spectra, photographs, hydration radius, UV-vis-NIR absorbance spectra, ultraphonic and photoacoustic images and H&E staining; Supplementary Figures S1-S8.
http://www.thno.org/v09p5214s1.pdf

Acknowledgements

References

1. Siegel RL, Miller KD, Jemal A. Cancer statistics. CA Cancer J Clin. 2017; 67: 7-30.
2. Siegel RL, Miller KD, Jemal A. Cancer statistics. CA Cancer J Clin. 2016; 66: 7-30.
3. Miller KD, Siegel RL, Lin CC, Mariotto AB, Kramer JL, Rowland JH, et al. Cancer treatment and survivorship statistics. CA Cancer J Clin. 2016; 66: 271-289.
4. Wang S, Lin J, Wang T, Chen X, Huang P. Recent advances in photoacoustic imaging for deep-tissue biomedical applications. Theranostics. 2016; 6: 2394-2413.
5. Ban Q, Bai T, Duan X, Kong J. Noninvasive photothermal cancer therapy nanoplatforms: via integrating nanomaterials and functional polymers. Biomater Sci. 2017; 5: 190-210.
6. Cai Y, Liang P, Tang Q, Yang X, Si W, Huang W, et al. Diketopyrrolopyrrole-triphenylamine organic nanoparticles as multifunctional reagents for photoacoustic imaging-guided photodynamic/photothermal synergistic tumor therapy. ACS Nano. 2017; 11: 1054-1063.
7. Song G, Wang Q, Wang Y, Lv G, Li C, Zou R, et al. A low-toxic multifunctional nanoplatform based on $Cu_9S_5@mSiO_2$ core-shell nanocomposites: combining photothermal- and chemotherapies with infrared thermal imaging for cancer treatment. Adv Funct Mater. 2013; 23: 4281-4292.
8. Kievit FM, Zhang M. Cancer nanotheranostics: Improving imaging and therapy by targeted delivery across biological barriers. Adv Mater. 2011; 23: H217-H247.
9. Yu MK, Park J, Jon S. Targeting strategies for multifunctional nanoparticles in cancer imaging and therapy. Theranostics. 2012; 2: 3-44.
10. Chen J, Yang M, Zhang Q, Cho EC, Cobley CM, Kim C, et al. Gold nanocages: a novel class of multifunctional nanomaterials for theranostic applications. Adv Funct Mater. 2010; 20: 3684-3694.
11. Zhang C, Zhao K, Bu W, Ni D, Liu Y, Feng J, et al. Marriage of scintillator and semiconductor for synchronous radiotherapy and deep photodynamic therapy with diminished oxygen dependence. Angew Chem Int Ed. 2015; 54: 1770-1774.
12. He L, Lai H, Chen T. Dual-function nanosystem for synergetic cancer chemo-/radiotherapy through ROS-mediated signaling pathways. Biomaterials. 2015; 51: 30-42.
13. Yang K, Hu L, Ma X, Ye S, Cheng L, Shi X, et al. Multimodal imaging guided photothermal therapy using functionalized graphene nanosheets anchored with magnetic nanoparticles. Adv Mater. 2012; 24: 1868-1872.
14. Park YI, Kim HM, Kim JH, Moon KC, Yoo B, Lee KT, et al. Theranostic probe based on lanthanide-doped nanoparticles for simultaneous in vivo dual-modal imaging and photodynamic therapy. Adv Mater. 2012; 24: 5755-5761.
15. Sheng Z, Hu D, Zheng M, Zhao P, Liu H, Gao D, et al. Smart human serum albumin-indocyanine green nanoparticles generated by programmed assembly for dual-modal imaging-guided cancer synergistic phototherapy. ACS Nano. 2014; 8: 12310-12322.
16. Zhou M, Chen Y, Adachi M, Wen X, Erwin B, Mawlawi O, et al. Single agent nanoparticle for radiotherapy and radio-photothermal therapy in anaplastic thyroid cancer. Biomaterials. 2015; 57: 41-49.
17. Huo D, Liu S, Zhang C, He J, Zhou Z, Zhang H, et al. Hypoxia-targeting, tumor microenvironment responsive nanocluster bomb for radical-enhanced radiotherapy. ACS Nano. 2017; 11: 10159-10174.
18. Davis JN, Medbery C, Sharma S, Pablo J, Kimsey F, Perry D, et al. Stereotactic body radiotherapy for centrally located early-stage non-small cell lung cancer or lung metastases from the RSSearch®patient registry. Rad Oncol. 2015; 10: 113.
19. Bentzen SM, Constine LS, Deasy JO, Eisbruch A, Jackson A, Marks LB, et al. Quantitative analyses of normal tissue effects in the clinic (quantec): an introduction to the scientific issues. Int J Rad Oncol Bio Phys. 2010; 76: S3-S9.
20. Sun X, Li XF, Russell J, Xing L, Urano M, Li GC, et al. Changes in tumor hypoxia induced by mild temperature hyperthermia as assessed by dual-tracer immunohistochemistry. Radiother Oncology J Eur Soc Therap Radio Oncol. 2008; 88: 269-276.
21. Goswami N, Luo Z, Yuan X, Leong DT, Xie J. Engineering gold-based radiosensitizers for cancer radiotherapy. Mater Horiz. 2017; 4: 817-831.
22. Yi X, Yang K, Liang C, Zhong X, Ning P, Song G, et al. Imaging-guided combined photothermal and radiotherapy to treat subcutaneous and metastatic tumors using iodine-131-doped copper sulfide nanoparticles. Adv Funct Mater. 2015; 25: 4689-4699.
23. Yu X, Li A, Zhao C, Yang K, Chen X, Li W. Ultrasmall semimetal nanoparticles of bismuth for dual-modal computed tomography/photoacoustic imaging and synergistic thermoradiotherapy. ACS Nano. 2017: 3990-4001.
24. Yong Y, Cheng X, Bao T, Zu M, Yan L, Yin W, et al. Tungsten sulfide quantum dots as multifunctional nanotheranostics for in vivo dual-modal image-guided photothermal/radiotherapy synergistic therapy. ACS Nano. 2015; 9: 12451-63.
25. Lu VM, McDonald KL, Townley HE. Realizing the therapeutic potential of rare earth elements in designing nanoparticles to target and treat glioblastoma. Nanomedicine. 2017; 12: 2389-2401.
26. Ma N, Wu F-G, Zhang X, Jiang Y-W, Jia H-R, Wang H-Y, et al. Shape-dependent radiosensitization effect of gold nanostructures in cancer radiotherapy: comparison of gold nanoparticles, nanospikes, and nanorods. ACS Appl Mater Inter. 2017; 9: 13037-13048.
27. Shen S, Chao Y, Dong Z, Wang G, Yi X, Song G, et al. Bottom-up preparation of uniform ultrathin rhenium disulfide nanosheets for image-guided photothermal radiotherapy. Adv Funct Mater. 2017; 27: 1700250.
28. Tang W, Dong Z, Zhang R, Yi X, Yang K, Jin M, et al. Multifunctional two-dimensional core–shell mxene@gold nanocomposites for enhanced photo–radio combined therapy in the second biological window. ACS Nano. 2019; 13: 284-294.
29. Horsman MR, Overgaard J. Hyperthermia: a potent enhancer of radiotherapy. Clin Oncol. 2007; 19: 418-426.
30. Liu J, Yang Y, Zhu W, Yi X, Dong Z, Xu X, et al. Nanoscale metal-organic frameworks for combined photodynamic & radiation therapy in cancer treatment. Biomaterials. 2016; 97: 1-9.
31. Huang X, El-Sayed IH, Qian W, El-Sayed MA. Cancer cell imaging and photothermal therapy in the near-infrared region by using gold nanorods. J Am Chem Soc. 2006; 128: 2115-2120.
32. Chen Z, Wang Q, Wang H, Zhang L, Song G, Song L, et al. Ultrathin PEGylated $W_{18}O_{49}$ nanowires as a new 980 nm-laser-driven photothermal agent for efficient ablation of cancer cells in vivo. Adv Mater. 2013; 25: 2095-2100.
33. Tian Q, Tang M, Sun Y, Zou R, Chen Z, Zhu M, et al. Hydrophilic flower-like CuS superstructures as an efficient 980 nm laser-driven photothermal agent for ablation of cancer cells. Adv Mater. 2011; 23: 3542-3547.
34. Ye S, Marston G, McLaughlan JR, Sigle DO, Ingram N, Freear S, et al. Engineering gold nanotubes with controlled length and near-infrared absorption for theranostic applications. Adv Funct Mater. 2015; 25: 2117-2127.
35. Li W, Rong P, Yang K, Huang P, Sun K, Chen X. Semimetal nanomaterials of antimony as highly efficient agent for photoacoustic imaging and photothermal therapy. Biomaterials. 2015; 45: 18-26.
36. Yong Y, Zhou L, Gu Z, Yan L, Tian G, Zheng X, et al. WS_2 nanosheet as a new photosensitizer carrier for combined photodynamic and photothermal therapy of cancer cells. Nanoscale. 2014; 6: 10394-10403.
37. Bashkatov AN, Genina EA, Kochubey VI, Tuchin VV. Optical properties of human skin, subcutaneous and mucous tissues in the wavelength range from 400 to 2000 nm. J Phys D: Appl Phys. 2005; 38: 2543-2555.
38. Cao Z, Feng L, Zhang G, Wang J, Shen S, Li D, et al. Semiconducting polymer-based nanoparticles with strong absorbance in NIR-II window for in vivo photothermal therapy and photoacoustic imaging. Biomaterials. 2018; 155: 103-111.
39. Wu Z-C, Li W-P, Luo C-H, Su C-H, Yeh C-S. Rattle-type $Fe_3O_4@CuS$ developed to conduct magnetically guided photoinduced hyperthermia at first and second nir biological windows. Adv Funct Mater. 2015; 25: 6527-6537.
40. Yang T, Tang Ya, Liu L, Lv X, Wang Q, Ke H, et al. Size-dependent Ag_2S nanodots for second near-infrared fluorescence/photoacoustics imaging and simultaneous photothermal therapy. ACS Nano. 2017; 11: 1848-1857.
41. Hui J, Li R, Phillips EH, Goergen CJ, Sturek M, Cheng JX. Bond-selective photoacoustic imaging by converting molecular vibration into acoustic waves. Photoacoustics. 2016; 4: 11-21.
42. Wang LV. Multiscale photoacoustic microscopy and computed tomography. Nat photonics. 2009; 3: 503-509.
43. Liu L, Qin H. Photoacoustic molecular imaging with functional nanoparticles. J Innov Opt Heal Sci. 2017; 10: 1730004.
44. Zhang C, Maslov K, Wang LV. Subwavelength-resolution label-free photoacoustic microscopy of optical absorption in vivo. Opt Lett. 2010; 35: 3195-3197.
45. Li L, Zhang HF, Zemp RJ, Maslov K, Wang LV. Simultaneous imaging of a lacZ-marked tumor and microvasculature morphology in vivo by dual-wavelength photoacoustic microscopy. J Innov Opt Heal Sci. 2008; 01: 207-215.
46. Cheng L, Liu J, Gu X, Gong H, Shi X, Liu T, et al. PEGylated WS_2 nanosheets as a multifunctional theranostic agent for in vivo dual-modal CT/photoacoustic imaging guided photothermal therapy. Adv Mater. 2014; 26: 1886-1893.
47. Kim G, Huang SW, Day KC, O'Donnell M, Agayan RR, Day MA, et al. Indocyanine-green-embedded PEBBLEs as a contrast agent for photoacoustic imaging. J Biomed Opt. 2007; 12: 044020-044028.

48. Uthaman S, Bom JS, Kim HS, John JV, Bom HS, Kim SJ, et al. Tumor homing indocyanine green encapsulated micelles for near infrared and photoacoustic imaging of tumors. J Biomed Mater Res B. 2016; 104: 825-834.

49. Jeon M, Song W, Huynh E, Kim J, Kim J, Helfield BL, et al. Methylene blue microbubbles as a model dual-modality contrast agent for ultrasound and activatable photoacoustic imaging. J Biomed Opt. 2014; 19: 016005-1-8.

50. Li W, Chen X. Gold nanoparticles for photoacoustic imaging. Nanomedicine (Lond). 2015; 10: 299-320.

51. Li A, Li X, Yu X, Li W, Zhao R, An X, et al. Synergistic thermoradiotherapy based on PEGylated Cu3BiS3 ternary semiconductor nanorods with strong absorption in the second near-infrared window. Biomaterials. 2017; 112: 164-175.

52. Moon H, Kumar D, Kim H, Sim C, Chang J-H, Kim J-M, et al. Amplified photoacoustic performance and enhanced photothermal stability of reduced graphene oxide coated gold nanorods for sensitive photoacoustic imaging. ACS Nano. 2015; 9: 2711-2719.

53. Cheng L, He W, Gong H, Wang C, Chen Q, Cheng Z, et al. PEGylated micelle nanoparticles encapsulating a non-fluorescent near-infrared organic dye as a safe and highly-effective photothermal agent for *in vivo* cancer therapy. Adv Funct Mater. 2013; 23: 5893-5902.

54. Xie C, Zhen X, Lei Q, Ni R, Pu K. Self-assembly of semiconducting polymer amphiphiles for in vivo photoacoustic imaging. Adv Funct Mater. 2017; 27: 1605397.

55. Lovell JF, Jin CS, Huynh E, Jin H, Kim C, Rubinstein JL, et al. Porphysome nanovesicles generated by porphyrin bilayers for use as multimodal biophotonic contrast agents. Nat Mater. 2011; 10: 324-332.

56. Wu J, You L, Lan L, Lee HJ, Chaudhry ST, Li R, et al. Semiconducting polymer nanoparticles for centimeters-deep photoacoustic imaging in the second near-infrared window. Adv Mater. 2017; 29:1703403.

57. Guo B, Sheng Z, Kenry K, Hu D, Lin X, Xu S, et al. Biocompatible conjugated polymer nanoparticles for highly efficient photoacoustic imaging of orthotopic brain tumors in the second near-infrared window. Mater Horiz. 2017; 4: 1151-1516.

58. Sun T, Dou JH, Liu S, Wang X, Zheng X, Wang Y, et al. Second near-infrared conjugated polymer nanoparticles for photoacoustic imaging and photothermal therapy. ACS Appl Mater Inter. 2018; 10: 7919-7926.

59. Tsai MF, Chang SHG, Cheng FY, Shanmugam V, Cheng YS, Su CH, et al. Au nanorod design as light-absorber in the first and second biological near-infrared windows for *in vivo* photothermal therapy. ACS Nano. 2013; 7: 5330-42.

60. Zhou J, Jiang Y, Hou S, Upputuri PK, Wu D, Li J, et al. Compact plasmonic blackbody for cancer theranosis in the near-infrared II window. ACS Nano. 2018; 12: 2643-2651.

61. In S, Orlov A, Berg R, García F, Pedrosa-Jimenez S, Tikhov MS, et al. Effective visible light-activated B-doped and B,N-codoped TiO2 photocatalysts. J Am Chem Soc. 2007; 129: 13790-13791.

62. Morawski AW, Janus M, Tryba B, Inagaki M, Kałucki K. TiO2-anatase modified by carbon as the photocatalyst under visible light. CR Chim. 2006; 9: 800-805.

63. Asahi R, Morikawa T, Ohwaki T, Aoki K, Taga Y. Visible-light photocatalysis in nitrogen-doped titanium oxides. Science. 2001; 293: 269-271.

64. Di Valentin C, Pacchioni G, Selloni A, Livraghi S, Giamello E. Characterization of paramagnetic species in N-doped TiO2 powders by EPR spectroscopy and DFT calculations. J Phys Chem B. 2005; 109: 11414-11419.

65. Di Valentin C, Finazzi E, Pacchioni G, Selloni A, Livraghi S, Paganini MC, et al. N-doped TiO2: theory and experiment. Chem Phys. 2007; 339: 44-56.

66. Teruhisa O, Takahiro M, Michio M. Photocatalytic activity of S-doped TiO2 photocatalyst under visible light. Chem Lett. 2003; 32: 364-365.

67. Chen D, Jiang Z, Geng J, Wang Q, Yang D. Carbon and nitrogen co-doped TiO2 with enhanced visible-light photocatalytic activity. Ind Eng Chem Res. 2007; 46: 2741-2746.

68. Gong J, Yang C, Pu W, Zhang J. Liquid phase deposition of tungsten doped TiO2 films for visible light photoelectrocatalytic degradation of dodecyl-benzenesulfonate. Chem Eng J. 2011; 167: 190-197.

69. Archana PS, Gupta A, Yusoff MM, Jose R. Tungsten doped titanium dioxide nanowires for high efficiency dye-sensitized solar cells. Phys Chem Chem Phys. 2014; 16: 7448-7454.

70. Teoh WY, Amal R, Mädler L, Pratsinis SE. Flame sprayed visible light-active Fe-TiO2 for photomineralisation of oxalic acid. Catal Today. 2007; 120: 203-213.

71. Sun X, Zhang YW, Du YP, Yan ZG, Si R, You LP, et al. From trifluoroacetate complex precursors to monodisperse rare-earth fluoride and oxyfluoride nanocrystals with diverse shapes through controlled fluorination in solution phase. Chem Eur J. 2007; 13: 2320-2332.

72. Štengl V, Bakardjieva S, Murafa N. Preparation and photocatalytic activity of rare earth doped TiO2 nanoparticles. Mater Chem Phys. 2009; 114: 217-226.

73. Yu N, Hu Y, Wang X, Liu G, Wang Z, Liu Z, et al. Dynamically tuning near-infrared-induced photothermal performances of TiO2 nanocrystals by Nb doping for imaging-guided photothermal therapy of tumors. Nanoscale. 2017; 9: 9148-9159.

74. Guo W, Guo C, Zheng N, Sun T, Liu S. CsxWO3 Nanorods coated with polyelectrolyte multilayers as a multifunctional nanomaterial for bimodal imaging- guided photothermal/photodynamic cancer treatment. Adv Mater. 2017; 29: 1604157.

75. Liu J, Han J, Kang Z, Golamaully R, Xu N, Li H, et al. In vivo near-infrared photothermal therapy and computed tomography imaging of cancer cells using novel tungsten-based theranostic probe. Nanoscale. 2014; 6: 5770-5776.

76. Cui X-Z, Zhou Z-G, Yang Y, Wei J, Wang J, Wang M-W, et al. PEGylated WS2 nanosheets for X-ray computed tomography imaging and photothermal therapy. Chinese Chem Lett. 2015; 26: 749-754.

77. Wang Y, Chen T, Mu Q. Electrochemical performance of W-doped anatase TiO2 nanoparticles as an electrode material for lithium-ion batteries. J Mater Chem. 2011; 21: 6006.

78. Zeng J, Wang Y, Li Y, Yang Q, Yin Q. Ferroelectric and piezoelectric properties of tungsten doped CaBi4Ti4O15 ceramics. J Electroceram. 2007; 21: 305-358.

79. Roper DK, Ahn W, Hoepfner M. Microscale heat transfer transduced by surface plasmon resonant gold nanoparticles. J Phys Chem C. 2007; 111: 3636-3641.

80. Guo C, Yu H, Feng B, Gao W, Yan M, Zhang Z, et al. Highly efficient ablation of metastatic breast cancer using ammonium-tungsten-bronze nanocube as a novel 1064 nm-laser-driven photothermal agent. Biomaterials. 2015; 52: 407-416.

81. Manikandan M, Hasan N, Wu HF. Platinum nanoparticles for the photothermal treatment of Neuro 2A cancer cells. Biomaterials. 2013; 34: 5833-5842.

82. Ren W, Yan Y, Zeng L, Shi Z, Gong A, Schaaf P, et al. A near infrared light triggered hydrogenated black tio2 for cancer photothermal therapy. Adv Healthcare Mater. 2015; 4: 1526-1536.

83. Yu CY, Xu H, Ji S, Kwok RT, Lam JW, Li X, et al. Mitochondrion-anchoring photosensitizer with aggregation-induced emission characteristics synergistically boosts the radiosensitivity of cancer cells to ionizing radiation. Adv Mater. 2017; 29: 1606167.

84. Cui FB, Li RT, Liu Q, Wu PY, Hu WJ, Yue GF, et al. Enhancement of radiotherapy efficacy by docetaxel-loaded gelatinase-stimuli PEG-Pep-PCL nanoparticles in gastric cancer. Cancer lett. 2014; 346: 53-62.

85. Corde S, Joubert A, Adam JF, Charvet AM, Le Bas JF, Estève F, et al. Synchrotron radiation-based experimental determination of the optimal energy for cell radiotoxicity enhancement following photoelectric effect on stable iodinated compounds. Br J Cancer. 2004; 91: 544-551.